Bioactive Materials 8 (2022) 435–448

Contents lists available at ScienceDirect

Bioactive Materials

journal homepage: www.sciencedirect.com/journal/bioactive-materials

Niobium carbide (MXene) reduces UHMWPE particle-induced osteolysis

Kuo-Yang Sun [a,1], Yizhang Wu [b,1], Jia Xu [c,1], Wenfang Xiong [d], Wei Xu [b], Jiawei Li [a], Ziying Sun [a], Zhongyang Lv [a], X.S. Wu [b], Qing Jiang [a], Hong-Ling Cai [b,**], Dongquan Shi [a,*]

[a] State Key Laboratory of Pharmaceutical Biotechnology, Department of Sports Medicine and Adult Reconstructive Surgery, Nanjing Drum Tower Hospital, The Affiliated Hospital of Nanjing University Medical School, 321 Zhongshan Road, Nanjing, 210008, Jiangsu, PR China
[b] Collaborative Innovation Center of Advanced Microstructures, Laboratory of Solid State Microstructures and School of Physics, Nanjing University, Nanjing, 210093, China
[c] Drum Tower of Clinical Medicine, Nanjing Medical University, Nanjing, 210008, Jiangsu, PR China
[d] Department of Gastroenterology, Nanjing Drum Tower Hospital, The Affiliated Hospital of Nanjing University Medical School, 321 Zhongshan Road, Nanjing, 210008, Jiangsu, PR China

ARTICLE INFO

Keywords:
Periprosthetic osteolysis
MXene
Niobium carbide
Osteoclastogenesis
Reactive oxygen species (ROS)

ABSTRACT

Joint replacement surgery is one of the orthopedic surgeries with high successful rates; however, wear debris generated from prostheses can ultimately lead to periprosthetic osteolysis and failure of the implant. The implant-derived particulate debris such as ultrahigh molecular weight polyethylene (UHMWPE) can initiate the local immune response and recruit monocytic cells to phagocytose particles for generating reactive oxygen species (ROS). ROS induces osteoclastogenesis and macrophages to secrete cytokines which ultimately promote the development of osteolysis. In this work, we develop the few-layered Nb_2C (FNC) as an antioxidant which possesses the feature of decreasing the production of cytokines and inhibiting osteoclastogenesis by its ROS adsorption. Moreover, local injection of FNC attenuates the UHMWPE-induced osteolysis in a mouse calvarial model. In sum, our results suggest that FNC can be used for treating osteolytic bone disease caused by excessive osteoclastogenesis.

1. Introduction

Total joint arthroplasty (TJA) is considered one of the highly successful surgeries in modern medicine, as it is the main strategy for patients with end stage arthritis. TJA can provide long-term improvement in quality of life, range of movement and function, arthritic pain relief [1]. However, the application and survivorship of TJA with the ultra-high molecular weight polyethylene (UHMWPE) bearing components has been limited due to periprosthetic osteolysis by wear of the UHMWPE [2]. The UHMWPE particles accumulating at the bone-implant interface ultimately leads to implant loosening and revision surgery [3]. Furthermore, age is one of known risk factors for osteolysis [4] and patients under the age of 65 will be the majority of the population for TJA in the United States between 2010 and 2030 [5,6]. Thus, patients undergoing TJA are predicted to increase making revision surgery a major concern.

Oxidative stress is one of the mechanisms that activates osteoclasts to enhance bone resorption [7,8]. With increased cyclic mechanical loading, a large amount of UHMWPE particles accumulate in interface between the bone and a prosthesis. Oxidative stress markers increase in the development of osteolysis [9]. It has been indicated that Reactive Oxygen Species (ROS) plays an important role in implant failure. The generation of UHMWPE debris from the articular surface of implant can initiate a local immune response that activates both resident and recruited macrophages to produce ROS that contain oxygen and unpaired electrons, including H_2O_2, O_2^-, and OH^-. Ultimately, ROS induce NF-κB signaling pathways resulting in inflammatory state of macrophages (M1) which are responsible for releasing pro-inflammatory cytokines such as interleukin-1 beta (IL-1β), interleukin-6 (IL-6) [10]. Moreover, UHMWPE debris are known to affect the activation of osteoclasts. There is much evidence show that periprosthetic osteolysis activates the RANK (receptor activator of nuclear factor kB (NF-kB)) and

Peer review under responsibility of KeAi Communications Co., Ltd.
** Corresponding author.
* Corresponding author.
E-mail addresses: hlcai@nju.edu.cn (H.-L. Cai), shidongquan@nju.edu.cn (D. Shi).
[1] These authors contributed equally to this work.

https://doi.org/10.1016/j.bioactmat.2021.06.016
Received 10 April 2021; Received in revised form 13 June 2021; Accepted 14 June 2021
Available online 1 July 2021

the RANK ligand (RANKL) signaling pathways [11]. UHMWPE particles also induce production of ROS which play as a second messenger in osteoclasts differentiation, and then ROS activate nuclear factor-κB (NF-κB) and mitogen-activated protein kinases (MAPKs) signaling pathways. Subsequently, transcription of nuclear factor of activated T-cells cytoplasmic 1 (NFATc1), a master regulator in osteoclastogenesis, is up-regulated and enhances osteoclastogenesis. Finally, bone resorption occurs. Recently, numerous studies have indicated that a platform carrying drugs [12,13], cells [14–17] and growth factors can promote tissue regeneration such as osteogenesis [18], but little attention has been given to its application in osteoclastogenesis, which are regulated by oxidative stress. In different biomedical areas, oxidative stress is usually considered a crucial target for intervening human pathophysiological processes which is involved in tumor development [19], viral infection [20,21], cardio vascular and neurological disease [22]. In the field of orthopedics, Monocyte/macrophage lineage cells are the principal activating factors of osteolysis. Therefore, a crucial point in limiting the periprosthetic osteolysis is to clearly eliminate inflammatory factors and ROS.

MXene is a large series consisted of ternary metal carbides/nitrides and donoted by $M_{n+1}X_nT_x$, where M is a transition metal such as Ti or Nb, X is carbon and/or nitrogen, and T are surface functional groups such as –O and –F. After the discovery by Gogotsi et al., in 2014, MXenes have widely been applied in different areas, such as electromagnetic wave absorption [23], Li–S battery [24], water desalination [25] and tissue engineering [26,27]. In addition, due to the excellent biocompatibility of MXenes (Ti_3C_2 and Nb_2C), applications of MXenes spread in many biomedical area. For example, Xu et al. [28] developed a simple and effective technique for fabricating FET transistors based on ultrathin conductive Ti_3C_2-MXene micropatterns for biosenors; Chen et al. [29] proved that Ti_3C_2 possess high photothermal-conversion and in *vitro*/in *vivo* photothermal ablation effects of tumors. Both of them display MXenes' distinctive properties in bio-application. Meanwhile, as to a recent work [30], single-layer Nb_2C could be utilized to prevent the Ionizing Radiation (IR)-induced injury which characterizes decreasing superoxide dismutase (SOD) activities and it can be excreted by various organs. This suggests that while MXenes have the same good biocompatibility [31,32] as graphene or other carbon-based materials, they also have the ability to spontaneously absorb a large amount of ROS. This is a unique advantage that graphene and carbon nanotubes do not have. Therefore, it is reasonable to speculate that ultrathin 2D Nb_2C can act as a potent antioxidant and suitable clinical agents with good biosafety for ROS related diseases.

In this work, we developed the ultra-thin 2D MXenes, and its ROS absorption capacity was evaluated compared bulk Nb_2C (BNC) with few-layered Nb_2C (FNC). Density functional theory (DFT) indicated that FNC exhibited an outstanding elimination of ROS and showed no obvious cytotoxicity in vitro. Especially, FNC inhibited inflammatory cytokine production and osteoclastogenesis via ROS scavenging and inhibition of its related cell signaling in vitro. Subsequently, we used UHMWPE particle-induced osteolysis model to testify the capacity of its ROS absorption. The Micro-CT results and histological assessments showed that osteolytic bone resorption on the surface of murine calvaria was significantly reduced after the FNC injection. Taken together, our results indicated that FNC can be used for preventing particle-induced periprosthetic osteolysis and other bone disease with excessive osteoclastogenesis.

2. Materials and methods

2.1. Materials

Nb_2AlC (>99%) powder was purchased from Feynman Nano Technology Co. Ltd. Lithium Fluoride (LiF, 99.9% metals basis) and Tetrapropylammonium hydroxide (TPAOH) aqueous solution were purchased from Alfa Aesar Chemicals Co. Ltd. Hydrochloric acid (HCl, 36.5–38.0 wt%) was purchased from Merck Pty. Ltd. All the chemical reagents were directly used without further purification.

2.2. Preparation of BNC and UNC

BNC was fabricated from Nb_2AlC by chemical exfoliation. In brief, 1.6 g LiF was slowly dissolved in 20 ml of 9 M HCl, stirred for 5 min, slowly added 1g Nb_2AlC (10 min), stirred at 45 °C for 24 h, then washed and dried overnight.

FNC was synthesized through TPAOH exfoliation from BNC for 72 h, then washed with DI water and centrifuged at 3500 Centrifuge for 5 min per minute, approximately 6–8 times to make the pH of the solution greater than 6.0. The deposit was dried overnight at 60 °C under vacuum.

2.3. Characterization of materials

Characterizations were explained by X-ray diffraction (XRD), X-ray photoelectron spectroscopy (XPS), Raman spectra, Atomic Force Microscope (AFM), Transmission Electron Microscope (TEM), Scanning Electron Microscope (SEM), Electron Spin Resonance (ESR) and specific surface area. Detailed process please see the *Supplied Experimental Section*, Supporting Information.

2.4. Theoretical calculations

Density Functional Theory (DFT) calculations were performed using the Vienna ab initio simulation package (VASP) [33]. The generalized gradient approximation (GGA) in the Perdew-Burke-Ernzerhof (PBE) form was used as exchange correlation functional. On-site Coulomb interaction to the Nb *d* orbitals was self-consistently calculated based on a linear response method. This calculation gives $U_{eff} = 2.6$ eV, which were used in our calculations. The projector-augmented wave (PAW) approach was used to describe the electron-core interactions and the cutoff energy for the plane wave basis set was 600 eV. The structure relaxations were performed using the conjugate gradient algorithm, until the total energies converged to 10^{-6} eV and the forces on the atoms were less than 0.01 eV $Å^{-1}$. In all calculations, the k-points were taken as $5 \times 5 \times 1$ and the integral of the Brillouin zone was calculated using the Γ-centered Monkhorst–Pack method. To compare the relative stabilities of the H configurations on a Nb_2C surface, we can define the adsorption energy of *n*th hydroxyl as $E_{ad} = E[Nb_2C\text{-}n\text{OH}] - E[Nb_2C\text{-}(n\text{-}1)\text{OH}] - E[\bullet\text{OH}]$.

2.5. Effect of FNC in UHMWPE-induced osteolysis model

The male 8-week-old C57BL/6J mice were used for UHMWPE-induced calvarial osteolysis model [34]. The animal experiments were approved by the Institutional Animal Care and Use Committee of the Affiliated Drum Tower Hospital of Nanjing University Medical School (20200602). In brief, the mice were anesthetized, and a 1 cm × 1 cm area of calvaria was exposed by a midline sagittal incision. The thirty mg particles were spread over the calvaria uniformly. After the wounds healed, the mice were divided into three groups: sham group, UHMWPE group, FNC group. FNC (20 mg/kg) was injected locally every two days in FNC group. After fourteen days, the mice were sacrificed for micro-computed tomography (CT) and histological analysis. First, the fixed calvarias were analyzed by using a high resolution micro-CT scanner (vivaCT 80, Switzerland). All samples were scanned according to the parameters (70 kVp, 57 μA, 4W). After reconstruction, the region of inetrest (ROI) were selected for quantitative analysis. Bone surface/Bone Volume (BS/BV), Bone Mineral Density (BMD), Bone Volume/Total Volume (BV/TV) were measured [35]. Second, the samples were decalcified in 10% EDTA for 3 weeks and then the sections were prepared for H&E and TRAP staining. The specimens were then examined and photographed under a high-quality microscope (ZEISS,

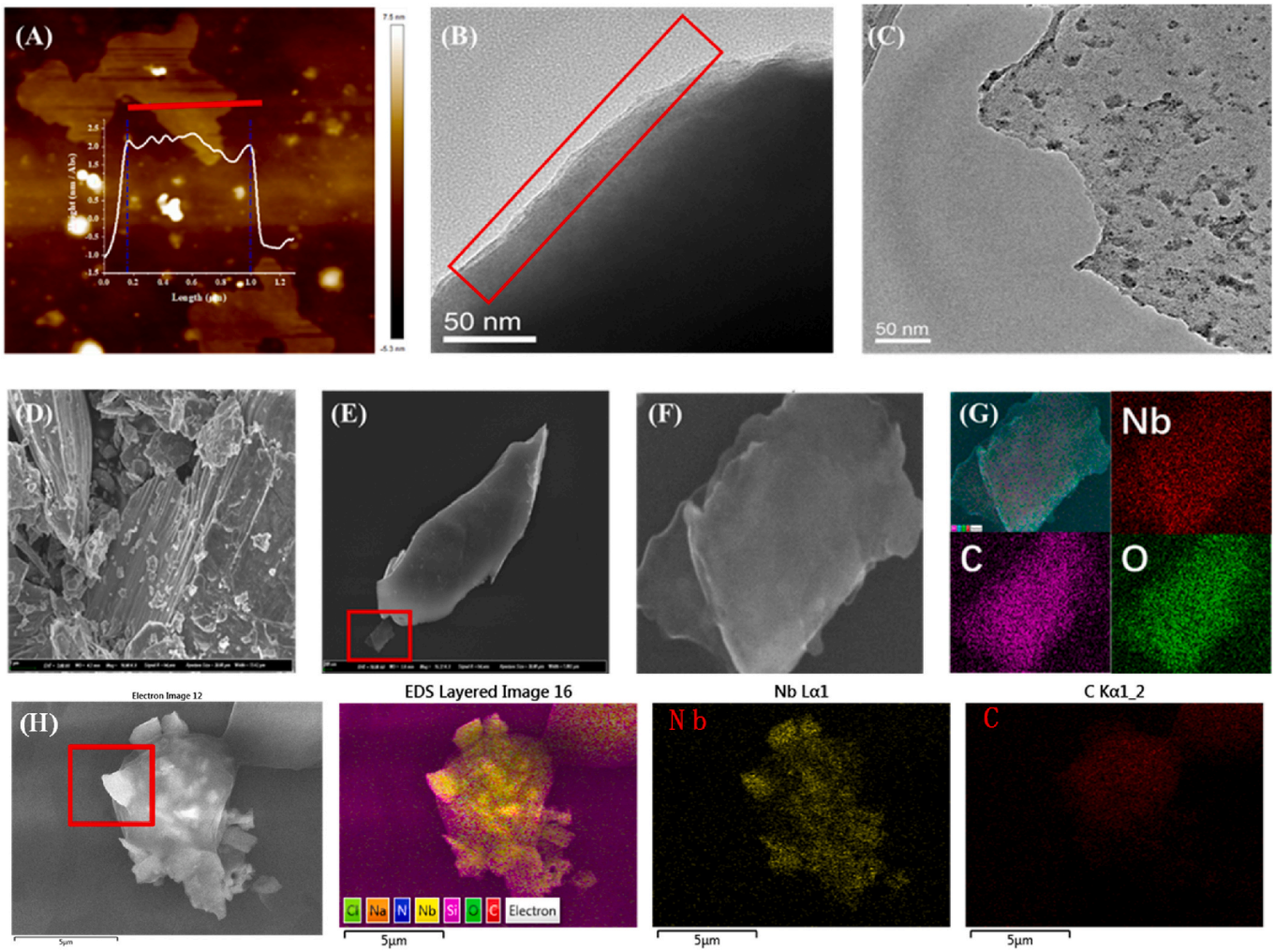

Fig. 1. The morphology of FNC. (A) AFM spectrum with cross-section profile and irregular polygon surrounding of FNC. The curve marks the change in horizontal thickness. (B) HRTEM image of BNC. The outline indicates a layered stack of edges (C) HRTEM image of FNC. (D) FESEM image of BNC. The scale bar is 1 μm. (E) FESEM image of FNC. The scale bar is 200 nm. (F) The corresponding partial enlarged image upon the outline and (G) Energy-dispersive spectroscopic element mapping of Nb, C and O elements. (H) SEM and the corresponding EDS spectrum after co-culturing FNC and RAW 264.7 cells for 6 h.

Germany).

2.6. Bone marrow-derived macrophages (BMMs) isolation and osteoclasts culture

Cells were isolated from the femur and the tibia of 8-week-old C57BL/6J mice. Cells were cultured with complete α-MEM medium for 24 h. Non-adherent cells, BMMs, were harvested and cultured with complete α-MEM medium containing 30 ng/ml M-CSF. Four days later, BMMs were further cultured with complete α-MEM medium containing with 30 ng/ml M-CSF and 50 ng/ml RANKL for 5 days. Culture media were replaced every two days.

2.7. The assay of bone resorption and F-actin ring formation

To perform resorption pits assay, bone slices were fixed with 4% paraformaldehyde and we removed mature osteoclasts completely by sonication. The resorption pits were observed by SEM (Quanta 200). The resorption pits were evaluated by using the Image J software. To perform F-actin ring formation assay, mature osteoclasts were fixed with 4% paraformaldehyde, and permeabilized with 0.1% Triton X-100 for 10 min. TRITC Phalloidin (YEASEN, China) were used to stain F-actin rings for 20 min at room temperature. The F-actin rings were observed using a fluorescence microscope (ZEISS, Germany), and numbers of F-actin rings were counted.

2.8. Cell viability assay

BMMs were seeded in 96-well plates at a density of 5×10^3 cells per well. BMMs were cultured in complete α-MEM medium supplemented with 30 ng/ml M-CSF in the presence of different concentrations of FNC (0, 25, 50, 100, 200 μg/ml) for 48 h. The cytotoxic effects of FNC were determined using the Live/Dead double staining assay and the CCK-8 assay. The optical density of the CCK-8 assay was measured at a wavelength of 450 nm (Thermo Fisher Scientific, USA). Moreover, Live/Dead staining was visualized using a fluorescence microscope (ZEISS, Germany).

2.9. ROS assay in vitro

BMMs were seeded into 6-well plates at a density of 1×10^5 cells per well. BMMs were pretreated with different concentrations of FNC for 3 h. BMMs were loaded with ROS sensitive dye DCFH-DA for 30 min before stimulation of RANKL. The intracellular ROS was measured by the ROS assay kit (Beyotime Technology Inc, China) and flow cytometer (BD Accuri C6 Plus, USA).

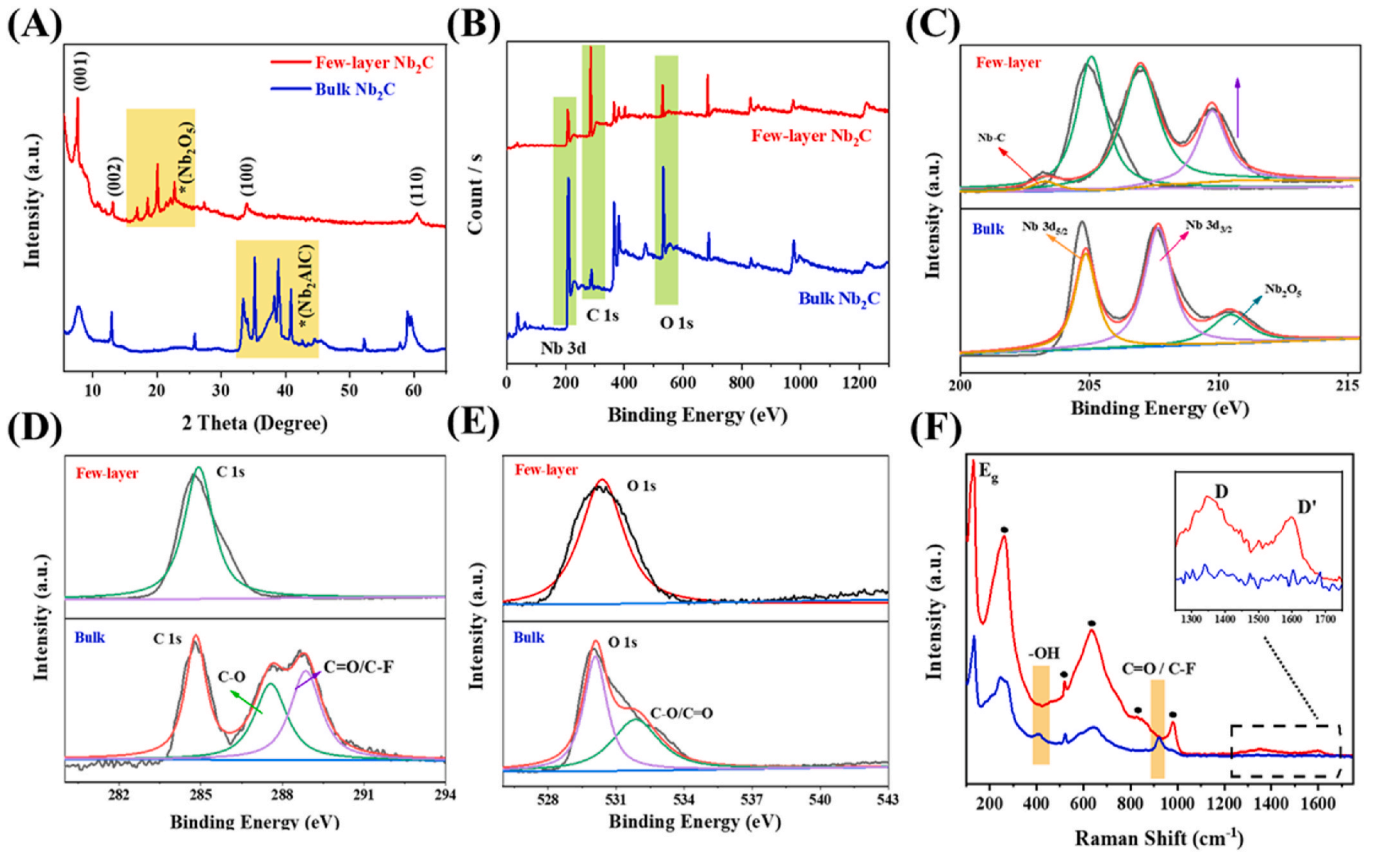

Fig. 2. Detailed structure of FNC. (A) XRD pattern of FNC and BNC. (B) XPS survey spectra of FNC and BNC. Highlighted sections correspond to Nb 3d, C 1s and O 1s, high-resolution XPS spectra of (C) Nb 3d; (D) C 1s; (E) O 1s. (F) Raman spectra of FNC and BNC at room temperature under 532 nm irradiation. The black dots mark the peaks of Nb_2O_5.

2.10. TRAP staining and activity

Osteoclasts were fixed in 4% formaldehyde and osteoclasts differentiation was evaluated with a TRAP detection kit (Sigma-Aldrich, USA). Stained osteoclasts were observed with an optical microscope (ZEISS, Germany) and quantified by Image-J software. Total protein was extracted and the TRAP activity was measured by the TRAP assay kit (Beyotime Technology Inc, China).

2.11. Quantitative real-time PCR (qPCR)

BMMs were seeded in six-well plates at a density of 1×10^5 cells per well. BMMs were cultured in complete α-MEM medium supplemented M-CSF and RANKL in the presence of FNC. Total RNA was extracted by using TRIzol reagent (Thermo Fisher Scientific, USA). Total RNA was used to synthesized cDNA using HiScript III RT SuperMix (Vazyme, China). A 20 μl mixture containing diluted cDNA was used to amplify using the ChamQ SYBR Color qPCR Master Mix (Vazyme, China) on the LightCycler 480 II (Roche, Switzerland). GAPDH was used as the house keeping gene. The primer sequences were described in Supplementary Table 1.

2.12. Western blot analysis

BMMs were seeded in six-well plates at a density of 1×10^5 cells per well. BMMs were co-cultured with FNC in the presence of M-CSF and RANKL. Total protein was extracted by using RIPA lysis buffer (Solarbio, China) which contains 1 mM phenylmethanesulfonyl fluoride (Solarbio, China) and 1 mM phosphatase inhibitor cocktail (Bimake, USA) for 15 min. The lysates were centrifuged at 12,000 rpm for 15 min. Total protein concentrations were determined by a BCA protein assay kit (Thermo Fisher Scientific, USA). SDS-PAGE on 10% gels were used to resolve equal amounts of protein lysate. Total protein were transferred to PVDF membranes (Millipore, USA). Membranes were blocked with 5% skimmed milk solution for 1 h and then membranes were incubated with specific primary antibodies overnight. The details of the primary antibody were described in Supplementary Table 2. Finally, membranes were washed and incubated with the proper secondary antibodies. The antibody reactivity was detected by the Tanon 5200 system (Bio Tanon, China) and signal intensities were analyzied by Image-J software.

2.13. Statistical analysis

Data were collected from three or more experiments. Using One-way analysis of variance (ANOVA) to test the differences between groups. The asterisks in the figures stands for the significance between groups. (*$P < 0.05$, **$P < 0.01$, ***$P < 0.001$, and ****$P < 0.0001$).

3. Results

3.1. The morphology and structure of FNC

Based on synthesis aims, we preliminarily infer that the Nb_2C is significantly thinner than the bulk Nb_2C (BNC) after Tetrapropylammonium hydroxide (TPAOH) peeling. The atomic force microscopic (AFM, Fig. 1A) presents that the stripped Nb_2C is an ultrathin 2D material with the thickness ranged from 2.6 nm to 3.2 nm, tentatively conforming to the thickness of five atomic layers of Nb_2C. Thus, we initially named it few-layered Nb_2C (FNC). When it comes to transmission electron microscope (TEM, Fig. 1B) of BNC, we can clearly see

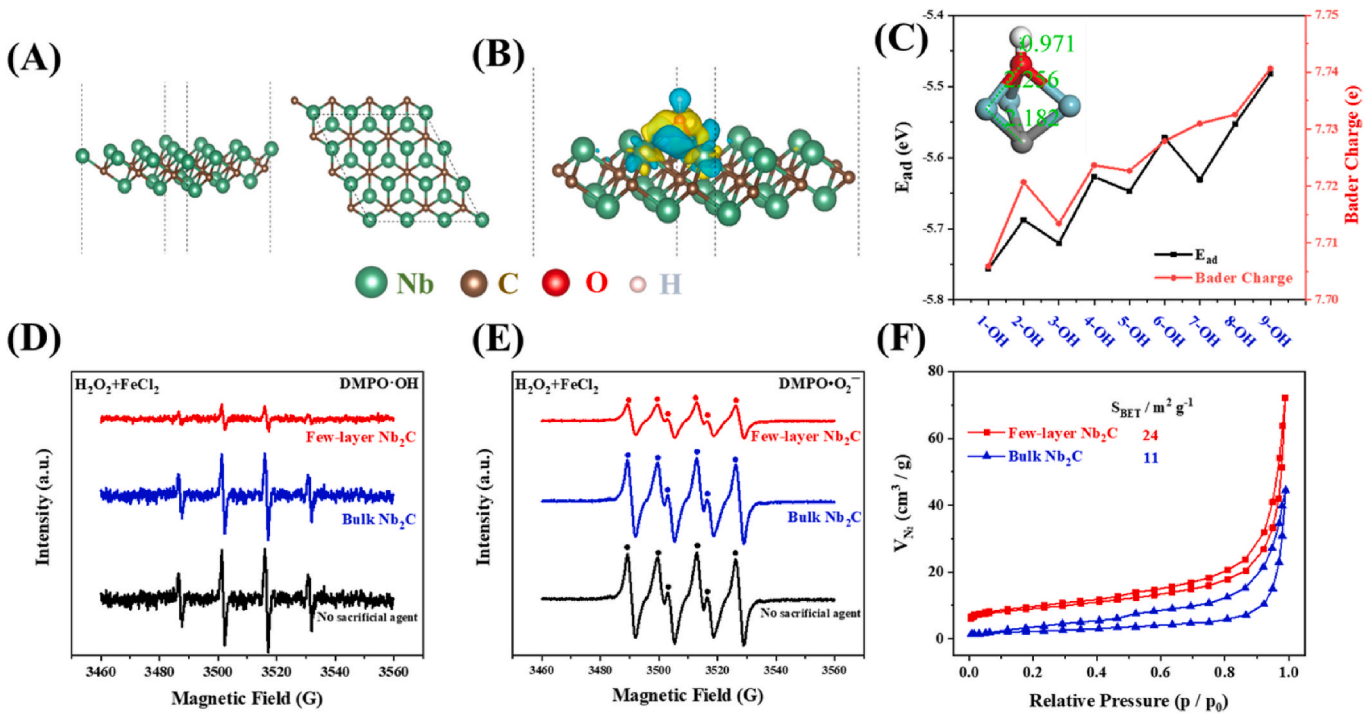

Fig. 3. DFT calculation and photoelectric performance of FNC. (A) Structure model of Nb_2C supercell. Brown, green, red, and white represent carbon, niobium, oxygen, and hydrogen atoms, respectively. (B) Isosurface of differential charge density of hydroxyl adsorption. Blue represents electron dissipation, and yellow represents electron aggregation. (C) The adsorption energy (left vertical axis) and the number of hydroxyl valence electrons (right vertical axis) change with the nth hydroxyl adsorption. The inset shows the length of each bond. ESR spectra of FNC and BNC (D) DMPO·O_2^- and (E) DMPO·OH adduct. (F) N_2 adsorption-desorption isotherms of the samples. The inset exhibits the S_{BET} of FNC and BNC. (For interpretation of the references to colour in this figure legend, the reader is referred to the Web version of this article.)

the layered stack at the edge of the nanosheets with the smooth surface. On the contrary, the surface of FNC (Fig. 1C) indicates the potholes and undulate surface, which is more likely to be the stacked N_2O_5. By the way, when the range of observation is adjusted from 50 nm to 1 μm and the mean of observation transforms to scanning electron microscopy (SEM, Fig. 1D–F, and Fig.1S), many suspension parts can be observed attached to the BNC surface, while the FNC surface is surprisingly flat. Meanwhile, elemental mapping of energy-dispersive X-ray spectroscopy (EDS, Fig. 1G) confirms the existence of FNC and shows the homogeneous distribution of niobium, carbon and oxygen elements. Taking into account this favorable condition, we co-cultured FNC and Raw 264.7 cells for 6 h before performing SEM and EDS (Fig. 1H). It can be seen that the FNC nanosheets have completely or partially entered the Raw 264.7 cells and are evenly distributed. This has laid the feasibility foundation for subsequent biological experiments.

In order to observe the structural and phase purity of as-synthesized Nb_2C, X-ray diffraction (XRD, Fig. 2A) was adopted using Cu-Kα radiations. In the view of XRD pattern, it can be seen that the (001) peak's width tends to narrow and the (100) and (110) become wider, which indicates that the disorder in the Z-direction decreases and the in-plane crystallinity deteriorates [36]. In addition, obvious characteristic peaks of Nb_2O_5 in FNC can be observed, but not in BNC, which can be assigned that FNC is easily oxidized as the groups (-F, –O) on the surface of FNC disappeared and the oxidation vacancies appeared [37].

The composition and overall crystalline structure of FNC and BNC were further investigated via X-ray photoelectron spectroscopy (XPS, Fig. 2B–E). The XPS survey indicates the apparent intensity damping on Nb 3d and O 1s, attributing to the thinner thickness of FNC, weakening the Nb responding and the detached oxygen and hydroxyl groups on the surface. The Nb 3d XPS spectrum shows two dominant signals belonging to Nb $3d_{3/2}$ (207.9 eV) and $3d_{5/2}$ (205.4 eV) [38]. Remarkably, the Nb–O peaks of NbO and Nb_2O_5 located at 203.2 eV and 210.6 eV, respectively, display an enhancement [39]. It is a convictive evidence that there are a large number of oxidized vacancies on the FNC surface. Furthermore, C–O single bond and C═O/-F bond have distinctly disappeared in FNC compared with that of BNC. The disappearance of –OH also revealed the exfoliation of suspension parts in BNC, with consistent of the above. It can be concluded that TPAOH stripping not only makes BNC exfoliation but also removes surface suspension groups (-F, –O, –OH) in BNC, leaving oxidized vacancies, as shown in Fig. S3.

Raman spectrum (Fig. 2F) of FNC exhibits two new sharp features at approximately 1350 cm^{-1} (D band) and 1620 cm^{-1} (D′ band). These inter-valley (D) and intra-valley (D′) defect-induced resonant scattering processes are the ones mainly responsible for electron decoherence in optics and transport phenomena in sp^2 carbons [40]. The appearance of D and D' resonant scattering implies the increased in-plane disorder, as well as the few-layered vertical structure in FNC. In addition, we can see that the characteristic peaks of C–O and C═O/-F have vanished while the intensity of Nb_2O_5 (marked with black dots) rise appreciably [41, 42], with consistent of the above conclusion. From above-mentioned analysis, FNC can be recognized as a MXene nanosheet without suspension parts at the terminal, attributing to the surface easily oxidized. It is conducive to supply the active sites for absorbing ROS, especially for hydroxyl radical [43].

3.2. FNC can suppress the ROS generation in mechanism

After a comprehensive understanding of the characterizations and structure, we envisioned that FNC would make a figure as a potent antioxidant and suitable clinical agents for ROS related diseases. We first demonstrate our concept on the basis of density functional theory (DFT) calculations. We build a 3 × 3 supercell of FNC (Fig. 3A) and DFT calculations are used to consider the hydroxyl adsorption process on the surface of FNC (Considering that the terminal of BNC are full of hydroxyl groups, the adsorption effect of BNC has not been calculated). The differential charge density (Fig. 3B) shows that when the hydroxyl group is

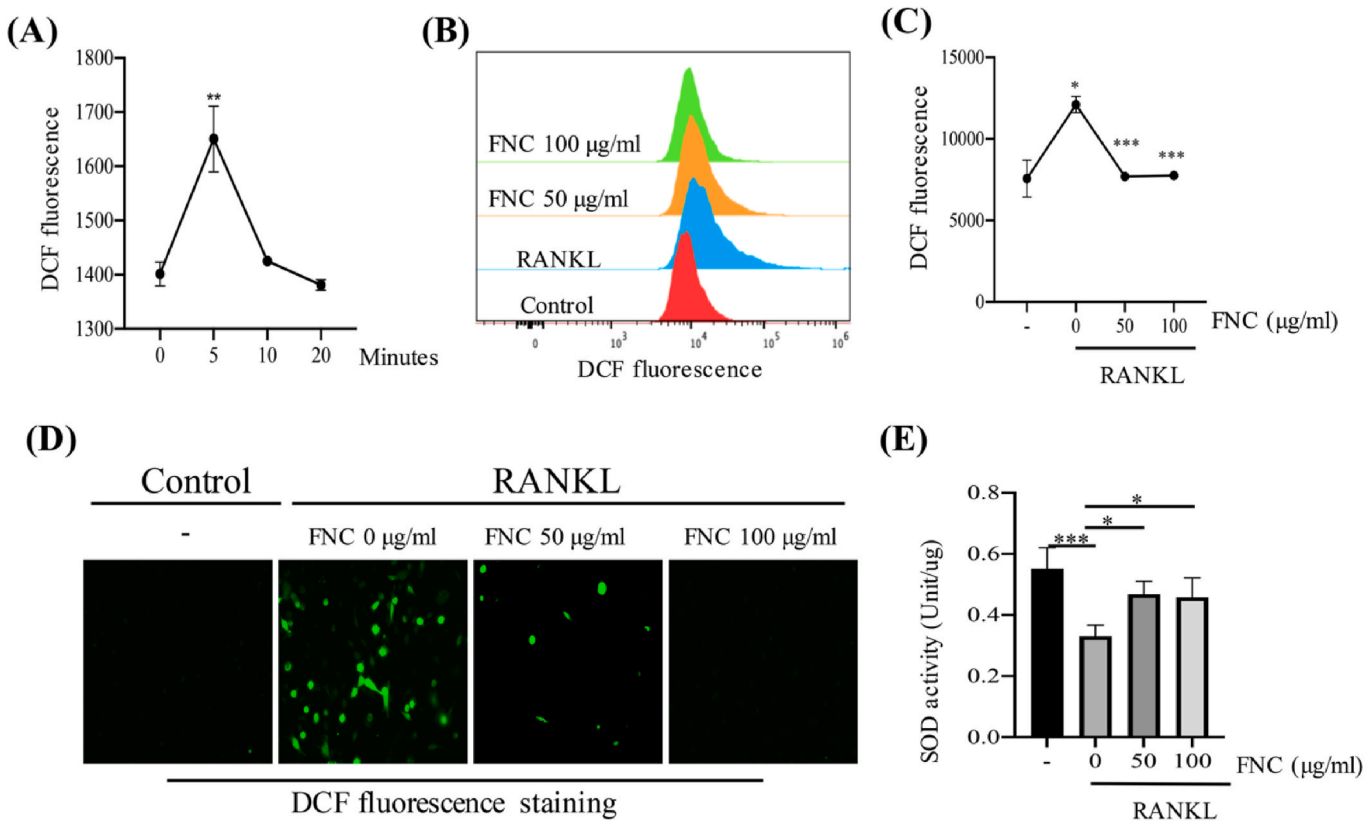

Fig. 4. FNC decreased ROS levels in BMMs with RANKL stimulation. (A) BMMs were treated with RANKL for different time intervals. The intracellular ROS levels were based on flow cytometry analysis with BMMs preloaded DCFH-DA ($n = 3$). (B–C) BMMs were pretreated with different concentrations of FNC for 3 h. DCF fluorescence was measured and quantified ($n = 3$). (D) The production of ROS was assayed by using fluorescence microscope. Green represents ROS levels. (E) BMMs were pretreated with different concentrations of FNC and total SOD activities were detected (n = 4). The asterisks in the figures stands for the significance between groups. (*P < 0.05, **P < 0.01, ***P < 0.001, and ****P < 0.0001). (For interpretation of the references to colour in this figure legend, the reader is referred to the Web version of this article.)

adsorbed on the surface of Nb_2C, electrons are transferred from Nb_2C to the hydroxyl group. We further studied the influence of the adsorption capacity of hydroxyl groups on the adsorption process (Fig. 3C). The results show that the adsorption energy generally increases with the increase of the adsorption capacity of hydroxyl groups, which means that the adsorption of hydroxyl groups on the surface of Nb_2C decreases. We also performed a Bader charge analysis [44]. As shown in Fig. 3C, the charge distributed on the hydroxyl group and the adsorption energy show the same trend. As the coverage of the hydroxyl group increases, the more electrons are distributed on each hydroxyl group. Additionally, it can be observed that with the amount of adsorbed hydroxyl groups increases, the binding energy stability gradually decreases, so the adsorption of ROS by Nb_2C is transient and limited, guiding us to conditionally apply this remarkable material in vivo.

To substantiate our DFT result, we first prepared ROS-generating reactor taking the advantage of Fenton reaction between hydrogen peroxide (H_2O_2) and $FeCl_2$ aqueous solution, which can directly produce a quantity of hydroxyl radicals (·OH). FNC and BNC had been supposed as the sacrificial agent. DMPO was normally regarded as a scavenger which trapped the ·OH and superoxide radicals ($\cdot O_2^-$) to transform the DMPO·OH and DMPO·O_2^- [45]. The entire process can be summarized in the following equations (1)–(4):

$$Fe^{2+} + H_2O_2 \rightarrow Fe^{3+} + OH^- + OH \quad (1)$$

$$e^- + O_2 \rightarrow \cdot O_2 \quad (2)$$

$$OH + DMPO \rightarrow DMPO{\cdot}OH \quad (3)$$

$$O_2^- + DMPO \rightarrow DMPO{\cdot}O_2^- \quad (4)$$

In view of these above-mentioned peculiarities, ESR was performed to evaluate the ROS absorption capacity of BNC and FNC. As is shown in Fig. 3D, FNC reveals the superior efficiency on the ·OH absorption compared with no sacrificial agent and BNC group. Meanwhile, what is surprising is that the suppression effect of FNC group is also significant for the high cytotoxic $\cdot O_2^-$ which is indirectly generated (Fig. 3E), owing to the inhibition of ·OH by FNC [32,46]. We found that FNC has a larger specific surface area (24 $m^2\ g^{-1}$ for FNC and 11 $m^2\ g^{-1}$ for BNC, Fig. 3F), assigned that the ultra-thin material can expose more internal layers and the corresponding in-plane aperture (Fig. S4), which can provide more active sites for the adsorption of ROS [31]. To sum up, we consider that FNC has potential to act as a better antioxidant for ROS related diseases.

3.3. FNC blocks RANKL-induced ROS production in vitro

To further investigate the effect of FNC, we first used Lipopolysaccharide (LPS)-induced inflammation model [47] for evaluating ROS absorption of BNC and FNC. Raw 264.7 cells were stimulated by LPS which was responsible for ROS production. After Raw 264.7 cells were treated with 10 ng/ml LPS for 3 h, the results of qPCR showed that Interleukin 1β (IL-1β) and Interleukin 6 (IL-6) were significantly decreased in FNC group (Figs. S4A–B). FNC revealed excellent ant-inflammatroy responses, but the tendency began to flatten out at higher concentrations (200 μg/ml). Furthermore, Raw 264.7 cells were loaded with ROS sensitive dye DCFH-DA and intracellular production of ROS was measured by a fluorescence microscope. Stimulation of Raw 264.7 cells resulted in the increasing intensity of DCFH fluorescence, while the raising production of ROS decreased by FNC and BNC treatment. Importantly, FNC treatment reduced ROS levels more efficiently

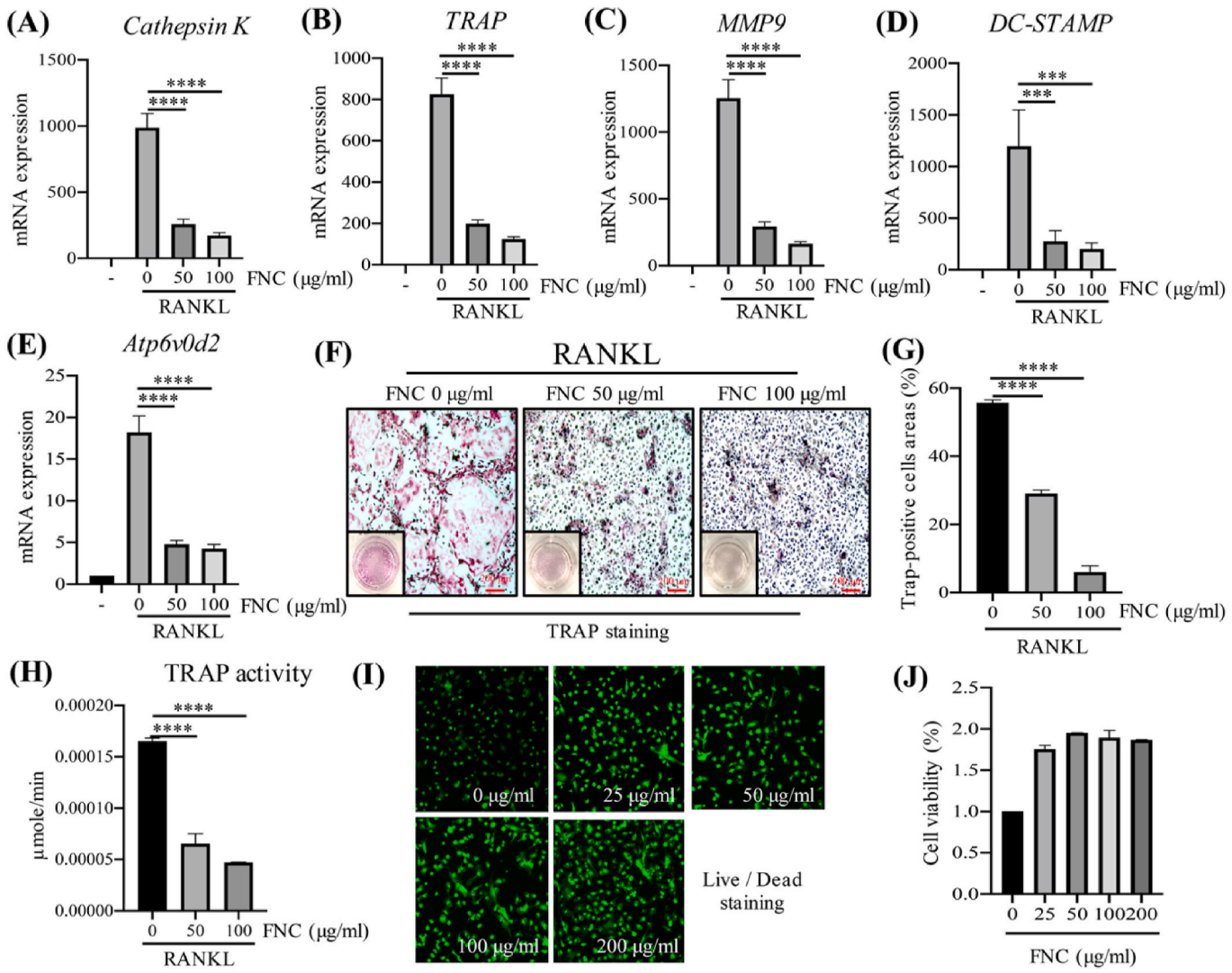

Fig. 5. FNC inhibited osteoclastogenesis in vitro. (A–E) BMMs cultured with different concentrations of FNC during osteoclastogenesis. The osteoclast-specific mRNA expression were measured by qPCR ($n = 3$). (F) BMMs were incubated with M-CSF and RANKL in the absence or presence of FNC for 5 days. The mature osteoclasts were confirmed by TRAP staining; (G) areas of TRAP-positive cell were calculated ($n = 3$) and (H) TRAP activity was measured ($n = 4$). (I) The Live/Dead cell double staining and (J) the CCK-8 assay were performed after BMMs were treated with various concentrations of FNC for 48 h ($n = 2$). The asterisks in the figures stands for the significance between groups. (*P < 0.05, **P < 0.01, ***P < 0.001, and ****P < 0.0001).

than BNC (Fig. S5). These results directed us to use FNC which was the preferred option in the subsequent tests.

Second, we induced production of ROS upon RANKL treatment in Bone marrow-derived macrophages (BMMs) during osteoclastogenesis. Although high levels of ROS is harmful, the appropriate level of ROS can serve as a second messenger in cell signaling such as osteoclastogenesis [8]. BMMs were loaded with ROS sensitive dye DCFH-DA and BMMs were stimulated with 50 ng/ml RANKL for the different time intervals. The flow cytometry analysis showed that ROS levels were increased at 5 min in response to RANKL and subsequently decreased to the basel level (Fig. 4A). Next we pretreated BMMs with different concentrations of FNC for 3 h. As shown in Fig. 4 B–C, FNC could reduce intracellular ROS significantly. Otherwise, the decreasing DCF fluorescence provided a consistent result which indicated excellent elimination of ROS by FNC (Fig. 4D). We also examined the total superoxide dismutase (SOD) activity which revealed a restoration effect in FNC group compared with RANKL group (Fig. 4E).

3.4. FNC protects against inflammation in vitro

Based on excellent ROS clearance of FNC and restoration of SOD activity in vitro, we next detected the effect of FNC on inflammation. BMMs were pretreated with different concentrations of FNC; then, BMMs were treated with 10 ng/ml LPS for 3 h. The results of qPCR showed that FNC inhibited several pro-inflammatory biomarkers of M1 macrophage including, IL-1β, IL-6, inducible nitric oxide synthase (iNOS), monocyte chemotactic protein 1 (MCP-1), nicotinamide adenine dinucleotide phosphate oxidases 1 (NOX1) (Figs. S6A–E). On the other hand, FNC can reduced secretion of IL-1β slightly and IL-6 markedly through ELISA kit detection (Figs. S6F–G). In inflammation, ROS are important for the maintenance of M1 type of macrophage polarization. Studies showed that ROS was the master regulator of pro-inflammatory gene expression in macrophages by activation of NF-κB signaling pathway [48]. Consistent with the results of the transcriptions and proteins level of inflammatory cytokines, the inhibition of the NF-κB signally pathway can be detected through Western blot analysis. It showed that FNC reduced the phosphorylation of NF-κB p65 and IκB kinase (IKK) which were responsible for immune and inflammatory

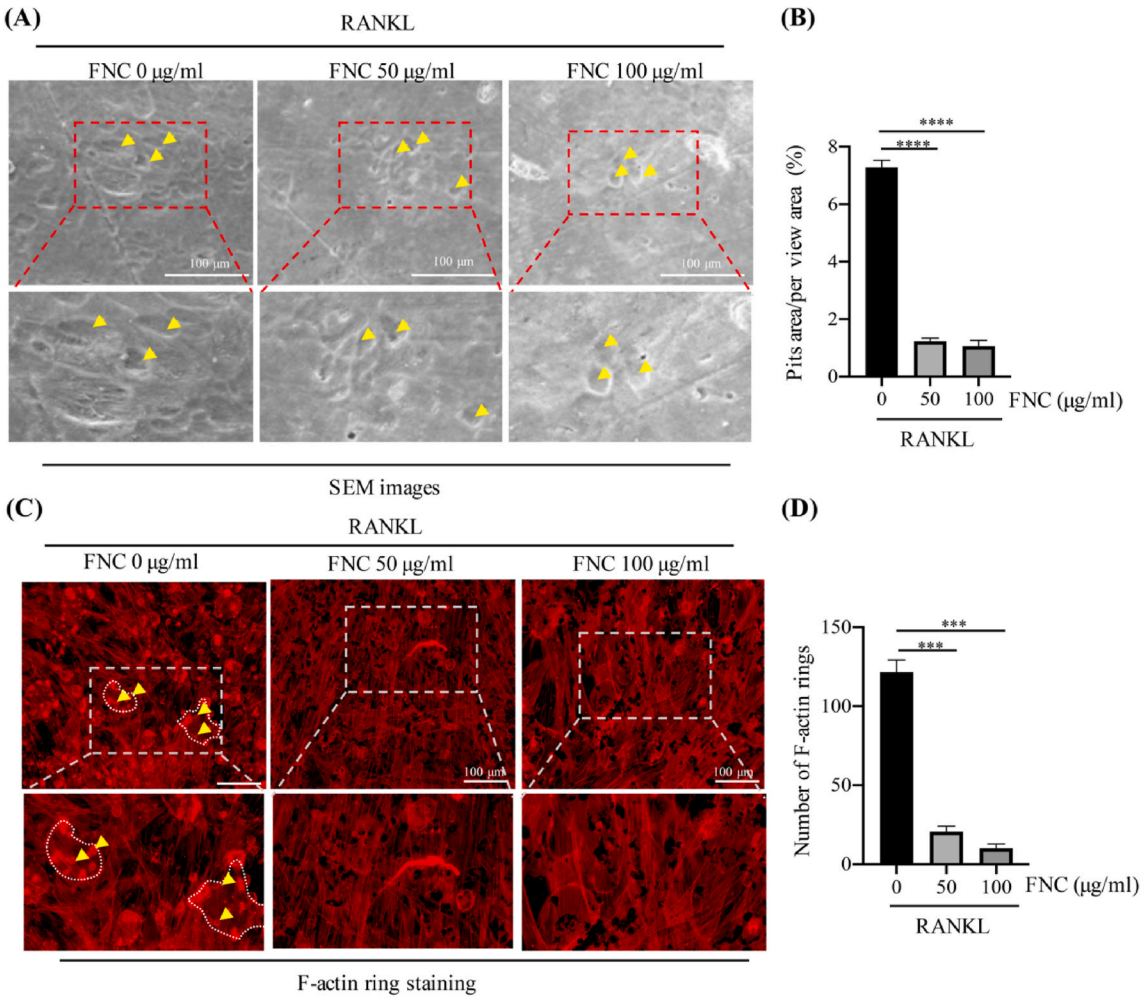

Fig. 6. Osteolytic bone resorption was inhibited by FNC treatment in vitro. (A) BMMs were co-cultured with different concentrations of FNC and stimulated with M-CSF and RANKL on the bone slices for 12 days. The surface of bone slices SEM images were shown, and yellow arrowheads represented bone resorption pits. (B) The resorption pits were quantified ($n = 3$). (C) The F-actin rings were stained after BMMs were treated with indicated concentrations of FNC during osteoclastogenesis. Red circle structure represented F-actin rings (yellow arrowheads), and the shape of mature osteoclasts were outlined (white dotted line). (D) The F-actin rings were counted ($n = 2$). The asterisks in the figures stands for the significance between groups. (*P < 0.05, **P < 0.01, ***P < 0.001, and ****P < 0.0001). (For interpretation of the references to colour in this figure legend, the reader is referred to the Web version of this article.)

responses (Figs. S6H–J). Taken together, FNC exhibited anti-inflammatory effect in vitro.

3.5. FNC inhibited osteoclastogenesis in vitro

Due to remarkable scavenging ROS ability and anti-inflammatory effect of FNC, we investigated whether FNC regulated osteoclast differentiation in RANKL-stimulated BMMs. For the assessment of FNC on osteoclast differentiation, BMMs were treated with 30 ng/ml M-CSF and 50 ng/ml RANKL in the presence of different concentrations of FNC for 4 days. The results of qPCR indicated that osteoclast-specific mRNA-expression including, cathepsin K, tartrate resistant acid phosphatase (TRAP), matrix metallopeptidase 9 (MMP9), Dendritic cell–specific transmembrane protein (DC-STAMP), d2 isoform of vacuolar ATPase V0 domain (Atp6v0d2) were all downregulated in the presence of FNC (Fig. 5A–E). Besides, we detected effect of FNC on osteoclast differentiation and found that the TRAP-positive cells, a specific marker of mature osteoclasts, were markedly decreased in the FNC group (Fig. 5F and G). Reduction of TRAP activity was also observed in FNC group compared with the RANKL group (Fig. 5H). To excluded the cytotoxic effects of FNC, we performed Live/Dead cell double staining and a CCK-8 assay to examine cell viability in vitro. As shown in Fig. 5I and J, the experiment data exhibited that FNC with different concentrations (from 0 to 200 μg/ml) had no toxicity to BMMs, and FNC even promoted the proliferation of BMMs [49,50]. In addition, FNC exhibited great biodegradability and biocompatibility, and FNC could be almost excreted by vital organs [30,31]. These results indicated that barely cytotoxic effects were observed and osteoclastogensis was significantly inhibited.

3.6. FNC attenuated osteoclastic bone resorption in vitro

Due to remarkable inhibition of osteoclast differentiation, we next focused on the effect of FNC on osteoclasts function. It was important to detect the mature osteoclasts which were considered as only cells that could absorb the bone. We used the pits formation assay to evaluate the bone resorption in the presence of different concentrations of FNC. BMMs were cultured on bone slices; then, BMMs were treated with M-CSF and RANKL with/without FNC for 12 days. After RANKL-induced osteoclasts differentiation, we harvested bone slices for SEM analysis. We found that the resorption pits were significantly decreased in the FNC group (Fig. 6A and B). In addition, a well-polarized F-actin ring represents the well-functioning osteoclasts during bone resorption [51]. Therefore, we performed the F-actin rings formation test to verify its formation and morphology in osteoclasts stained with TRITC Phalloidin.

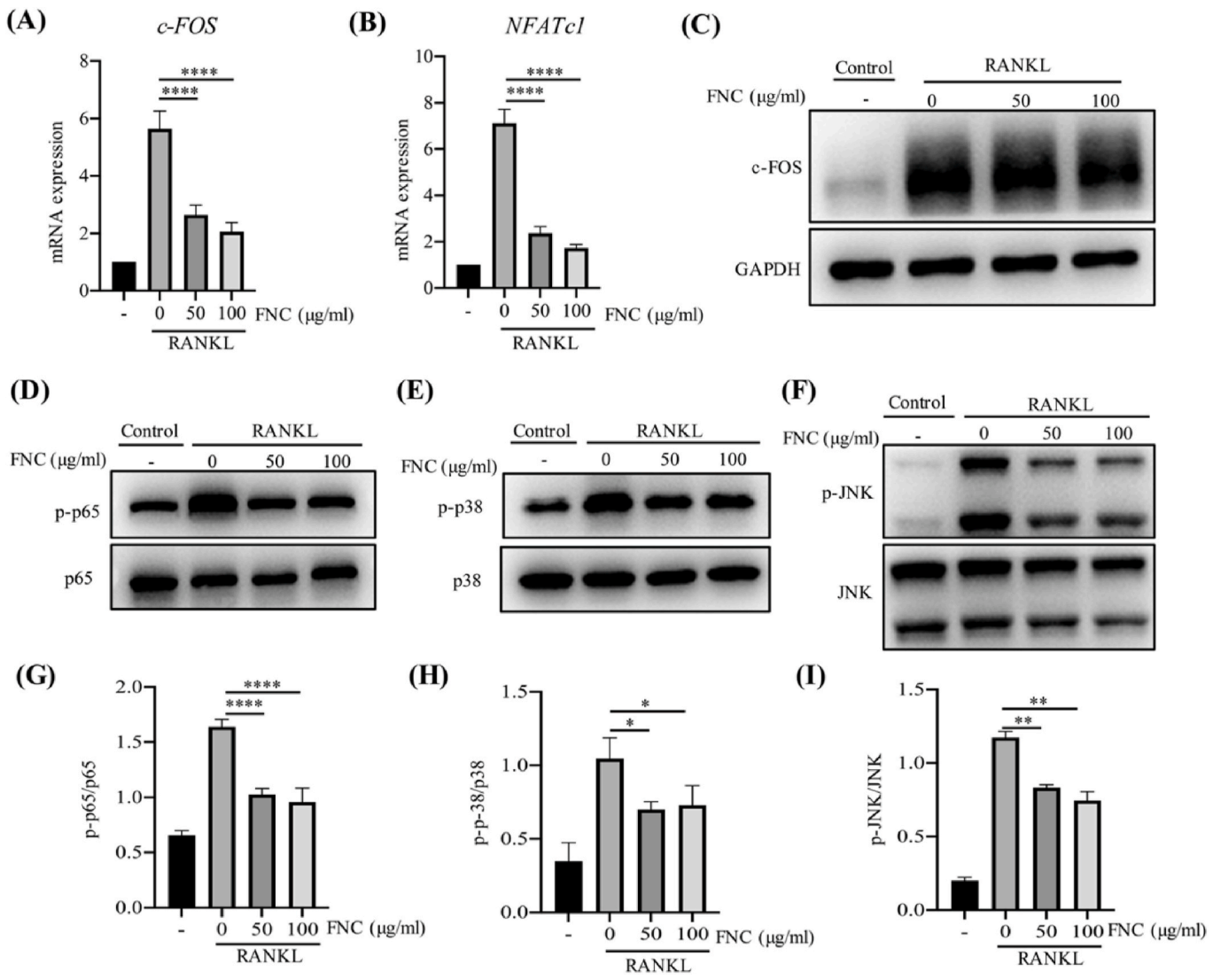

Fig. 7. FNC inhibited osteoclast related signal pathway. (A–B) Effect of FNC on BMMs stimulated with M-CSF and RANKL. The main osteoclast-specific regulator mRNA were detected after FNC treated ($n = 3$). (C) The osteoclast-specific regulators were detected at protein levels. (D–F) The downstream pathway NF-κB and MAP kinase activation were evaluated by Western blot, and (G–I) their activation were quantified ($n = 3$). The asterisks in the figures stands for the significance between groups. (*P < 0.05, **P < 0.01, ***P < 0.001, and ****P < 0.0001).

The results showed that FNC pretreatment dramatically disrupted the structures and reduced numbers of F-actin rings (Fig. 6C and D). Taken together, our findings showed that the function of mature osteoclasts was attenuated evidently.

3.7. FNC inhibited osteoclastogenesis via dampening related signal pathways

Next, we further investigated the mechanism of FNC on osteoclast differentiation. Previous studies have indicated that the NF-κB and MAPKs signaling pathways are involved in osteoclast differentiation [52]. First, RANKL potently induced master regulators of osteoclastogenesis such as NFATc1 and c-FOS, while the upregulation of NFATc1 and c-FOS were strongly suppressed in the presence of FNC (Fig. 7A–C). Second, we found that the phosphorylation of p65, p38, JNK, ERK(1/2) were increased in 15 min. However, their phosphorylation were inhibited by FNC treatment except for ERK(1/2) (Fig. 7D–F). Quantification of their phosphorylation also confirmed that FNC can significantly can down-regulate the NF-κB and MAPKs signaling pathways (Fig. 7G–I).

3.8. FNC inhibited osteoclastogenesis in UHMWPE particles-induced osteolysis model

To explore the effect of FNC on periprosthetic osteolysis, we used a murine calvaria model which used UHMWPE particles to induce osteolysis (Fig. 8A). When the surgical wound was healed, we locally injected FNC (20 mg/kg) to the bone resorption sites (Fig. 8B). The micro-CT scans and 3D reconstruction were used to evaluate the bone resorption. Extensive bone resorption was found in the UHMWPE group compared with the sham group. The FNC group showed that bone resorption was attenuated significantly (Fig. 8C and D). Bone parameters such as Bone surface/Bone Volume (BS/BV), Bone Volume/Total Volume (BV/TV), Bone Mineral Density (BMD) were also measured. The BS/BV showed that the erosion of calvaria was significantly increased in the UHMWPE group compared with sham group, while FNC injection could significantly decreased the BS/BV (Fig. 8E). Furthermore, we also confirmed that FNC injection significantly increased the BV/TV and BMD in the UHMWPE group compared with FNC group (Fig. 8F and G).

Hematoxylin and eosin (H&E) staining showed that there were less inflammatory responses and osteolytic changes in the sham group. In the UHMWPE group, inflammatory responses and osteolytic changes had

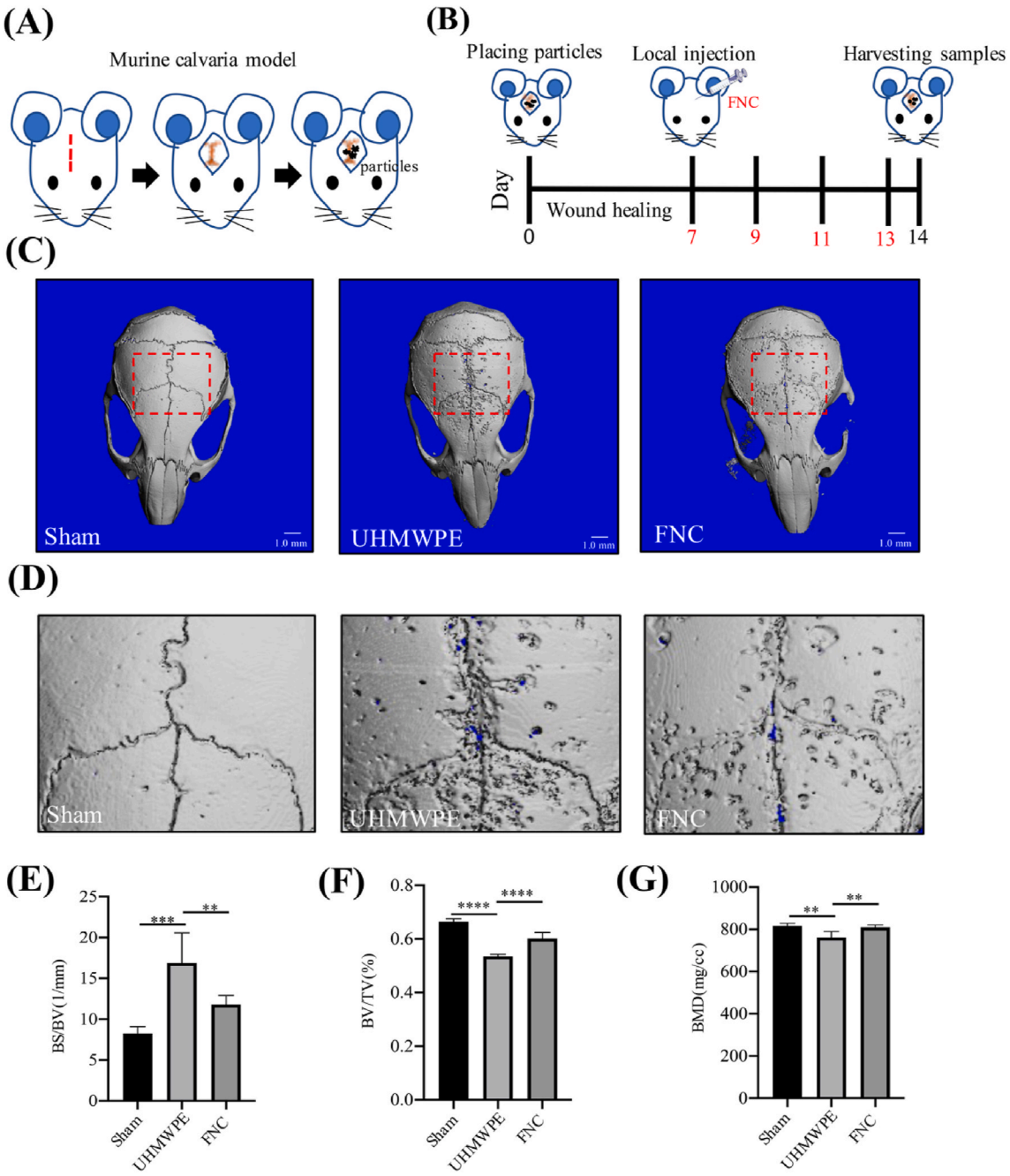

Fig. 8. FNC therapy in mice with UHMWPE-induced osteolysis. (A) The experimental murine osteolysis model. The surface of calvaria was exposed by a midline sagittal incision. Osteolysis was induced by placing UHMWPE particles on the surface for 14 days. (B) The experimental FNC treatment protocol. After wound was recovery, local injection was performed (red numbers). (C) 3D reconstruction was performed, and (D) the corresponding partial osteolytic area was enlarged. (E–G) Region of interest was measured and the osteolytic area was quantified into bone parameters ($n = 5$). The asterisks in the figures stands for the significance between groups. (*P < 0.05, **P < 0.01, ***P < 0.001, and ****P < 0.0001).

clearly occurred, whereas the FNC-treated group exhibited few inflammatory responses and osteolytic changes (Fig. 9A). TRAP staining exhibited more TRAP positive cells on the eroded bone surface in the UHMWPE group compared with the sham group; however, osteoclasts were obviously reduced in the FNC-treated group (Fig. 9B). Furthermore, our results indicated that there were no obvious toxic effect in vitro (Fig. 5I and J) and vivo (Fig. S7).

4. Discussion

TJA is widely used to treat the end-stage joint disease. However, UHMWPE wear particles are unavoidable and particle-induced osteolysis is the main cause of the implant loosening in joint replacement. As joint replacements are being extended to more active individuals who will potentially live for many decades longer, the debris in the joint will be the major concerns in the future. Although many advances have been made in agents, bearing materials, implant technologies, revision surgeries, the wear of implant has still been a series medical problem. In general, large amounts of particles-induced oxidative stress are gradually created around the implants. Moreover, ROS was reported that it was regarded as an upstream factor in the osteolysis cascade and inflammation. Therefore, it is urgent to find a new material which possessed the potential of inhibiting osteoclastogenesis and application of UHMWPE modification for decreasing wear rate.

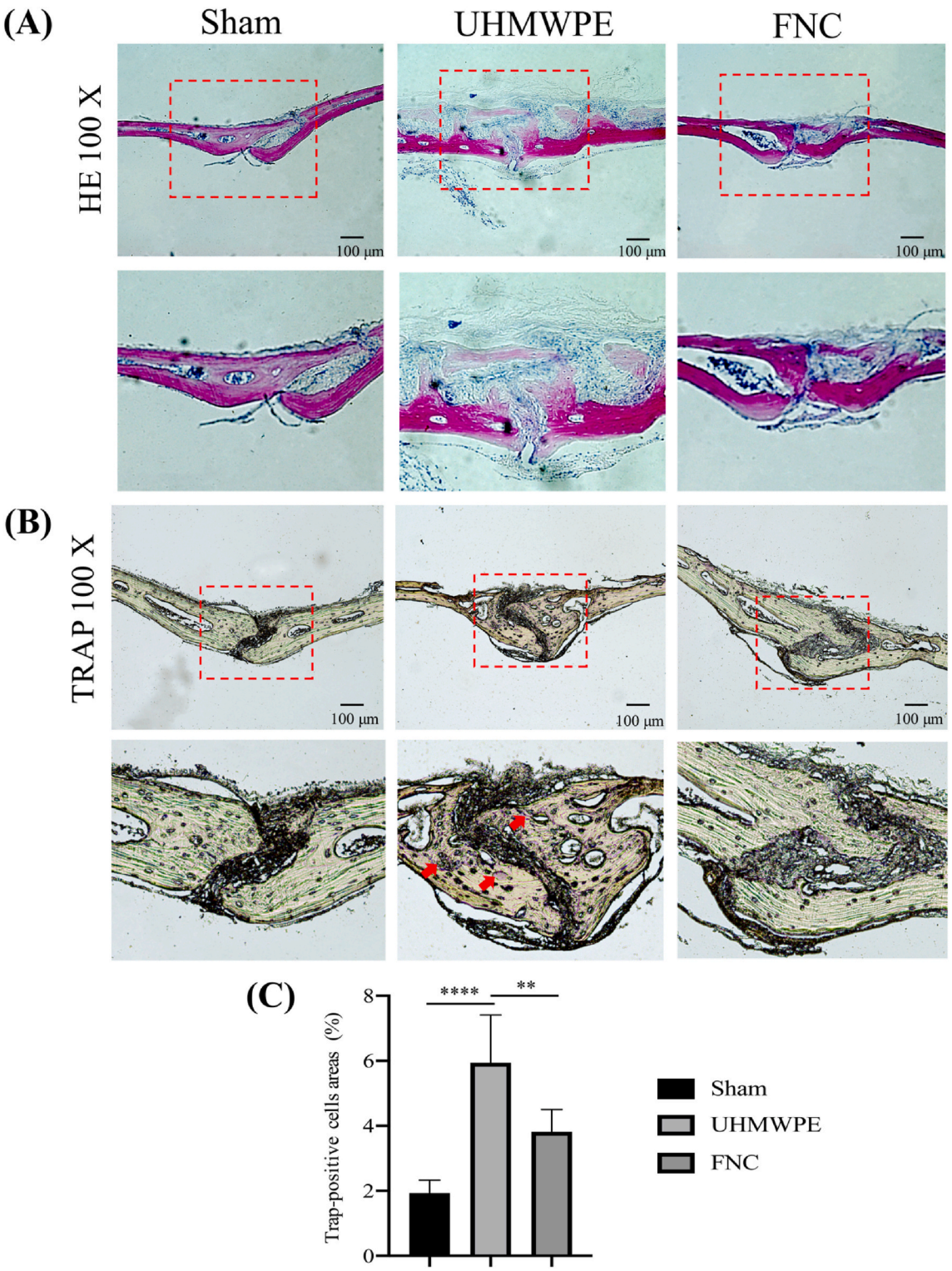

Fig. 9. Histological assessment of FNC on UHMWPE-induced osteolysis. (A) H&E staining (B) TRAP staining were performed, and the corresponding areas were enlarged. (C) TRAP positive areas were quantitated (n = 3). The red arrowheads indicated the TRAP positive osteoclasts. The upper space was outer space of calvaria, the lower space was inner space of calvaria. The asterisks in the figures stands for the significance between groups. (*P < 0.05, **P < 0.01, ***P < 0.001, and ****P < 0.0001). (For interpretation of the references to colour in this figure legend, the reader is referred to the Web version of this article.)

Currently, the mechanism which is associated with osteolysis in implant loosening focuses on the osteoclastogenesis. Osteoclastogenesis is a multistep process that includes recruitment of osteoclast precursors, multinucleated osteoclasts formation, activation of mature osteoclasts, and survival of osteoclasts in sequence. There were other studies to provide evidence that recruitment of osteoclast precursors and the flowing differentiation were the crucial roles in osteoclastogenesis rather than maintaining survival of osteoclasts [53]. Moreover, ROS was considered as the factor which promotes osteoclastogenesis in the early stage. Under the physiological state, the level of cellular ROS is

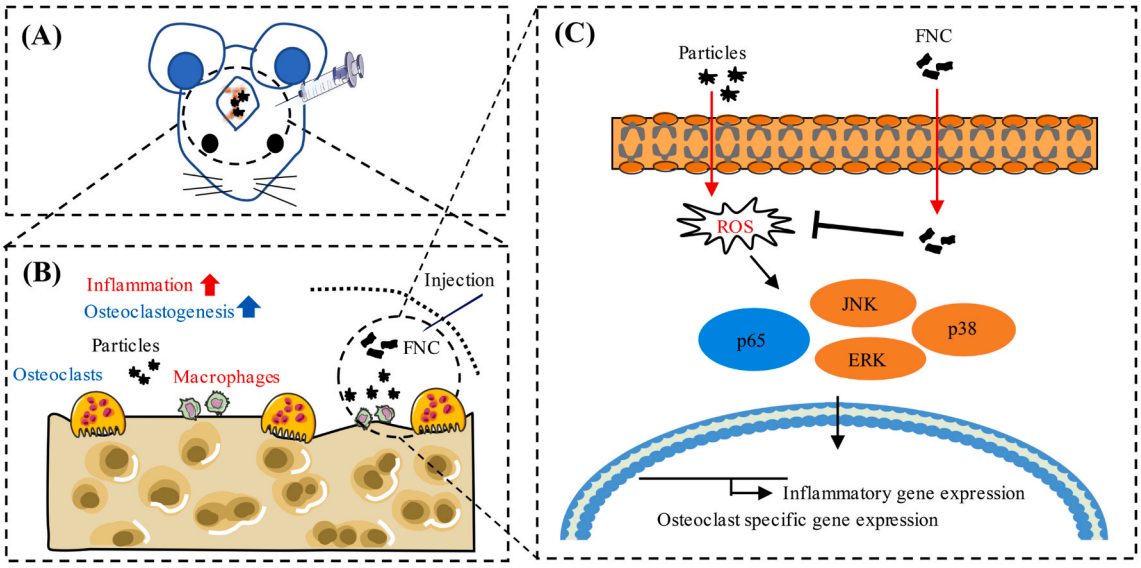

Fig. 10. Schematic diagram of FNC inhibited inflammation and osteoclastogenesis. (A) Local injection of FNC at osteolytic sites. (B) Materials interaction between macrophages and osteoclasts that influenced inflammation and osteoclastogenesis. (C) FNC were phagocytosed, and FNC exhibited effect of ROS adsorption. Subsequently, the inflammatory and osteoclast specific gene were downregulated.

modulated by cellular processes in a dynamic equilibrium; however, external stimuli including RANKL, M-CSF stimulate formation of ROS to trigger osteoclast differentiation and activation. Consistent with previous studies, our results also indicated that RANKL-induced production of ROS increased to a maximum level in a short time [8,54], activating downstream pathways to initiate induction of NFATc1, which is the key regulator during osteoclastogenesis. We speculated that production of ROS decreasing to the basel level could be a self-protection mechanism of cells for maintaining the level of cellular ROS. These pathological characteristics of osteolysis indicate that ROS can control cell development or differentiation and intervention of early stage osteoclastogenesis may be consider as an optimal way to treat periprosthetic osteolysis. Here, we designed FNC as a candidate for the ROS adsorption agent and the additive of UHMWPE in the future.

In our study, we synthesized FNC by chemical exfoliation from BNC. Although FNC is solid-phase, FNC has relatively good dispersibility because of its ultrathin thickness. It endows FNC nanosheets a suspension in DI water came from the surface tension of water for further experiments. Our results indicated that inflammation or osteoclastogenesis were inhibited by the ROS clearance of FNC under LPS or RANKL stimulation in vitro. FNC also inhibited NF-kB and MAPKs signalling pathways that has been shown to regulate the specific genes required for inflammation or bone resorption. In mechanism, FNC reveals a superior specific surface area and little –F/-O suspend on the surface, simultaneously supplying more reaction sites and vast oxidized vacancies to harvest the hydroxyl radical. The antioxidant mechanism of FNC is different than most of antioxidant pharmaceuticals which usually target proteins associated with oxidative stress during osteoclast differentiation. Importantly, FNC directly scavenge ROS and may avoid unwanted off-target effects of antioxidant pharmaceuticals. To further confirm the therapeutic efficacy of FNC, we locally injected FNC to osteolytic sites in the UHMWPE-induced osteolysis model. Histological assessments and TRAP-staining indicated that FNC reduced osteoclast formation and osteolytic changes. Consistent with what we expected, FNC can potentially prevent periprosthetic osteolysis and other ROS-related diseases.

However, some limitations existed in our study. First, the long-term biosafety of FNC has not been assessed. Although several studies have demonstrated that FNC possessed biodegradable [30,55], most studies were based on cell experiments or histology of short-term animal models. Second, the murine calvaria model exhibited the acute inflammatory effect for mimicking osteolysis rather than chronic inflammatory effect. It was also lacking the mechanical loading factor, indicating that it could influence biological responses of local progenitor cells [56]. Third, it is difficult to make macrophages contact with UHMWPE particles and makes a stable inflammatory model in vitro because of smaller density (0.97 g/cm^3) of UHMWPE. However, Toll-like receptors (TLRs) can be stimulated in early inflammatory responses. Studies found that expression of TLRs including, TLR 2, 4, 5, and 9 were increased in periprosthetic tissues [57] and polyethylene derivatives increased their affinity for TLRs [58]. Therefore, we replaced UHMWPE particles with LPS credited to LPS as regarded to the ligand for Toll-like receptor 4 (TLR4) in most cell such as Macrophages [59].

4. Conclusion

We successfully demonstrated FNC was highly effective in scavenging ROS, exploring the novel application of FNC for treating ROS related diseases (Fig. 10) and further research of UHMWPE modification rather than the conventional function of photodynamic therapy (PDT)/photothermal therapy (PTT) for cell killing. Our results clearly demonstrated ROS adsorption of FNC in mechanism and verified inhibition of osteoclastogenesis in vitro. Furthermore, results provided strong evidence that osteolysis was attenuated under UHMWPE stimulation in vivo. Our work will inspire promising strategies for developing new medical materials.

Appendix A. Supplementary data

Supplementary data to this article can be found online at https://doi.org/10.1016/j.bioactmat.2021.06.016.

Credit author statement

Kuo-Yang Sun, Yizhang Wu, conceived and designed the experiments. Kuo-Yang Sun, Yizhang Wu, Jia Xu, performed experiments, analyzed and interpreted the results. Wei Xu undertook the theoretical calculation section. Wenfang Xiong assisted the animal experiments, and cells isolation and culture expansion. Jiawei Li, Ziying Sun, Zhongyang Lv assisted the cell experiments. Kuo-Yang Sun, Yizhang Wu, Wei Xu wrote the manuscript. X.S. Wu, Qing Jiang, Hong-Ling Cai and Dongquan Shi oversaw the work.

Funding

This work was supported by National Key R&D Program of China (2018YFC1105904, 2016YFA0201104), National Science Foundation of China (81772335, 81941009, 81802196, 11874200), Natural Science Foundation of Jiangsu Province, China (BK20180127), Jiangsu Provincial Key Medical Talent Foundation, Six Talent Peaks Project of Jiangsu Province (WSW-079).

Competing interests

The authors declare that they have no competing interests.

Data and materials availability

All data are available in the main text or the supplementary materials.

References

[1] O. Ethgen, O. Bruyere, F. Richy, C. Dardennes, J.Y. Reginster, Health-related quality of life in total hip and total knee arthroplasty. A qualitative and systematic review of the literature, J Bone Joint Surg Am 86 (5) (2004) 963–974, https://doi.org/10.2106/00004623-200405000-00012.

[2] J.M. Anderson, A. Rodriguez, D.T. Chang, Foreign body reaction to biomaterials, Semin. Immunol. 20 (2) (2008) 86–100, https://doi.org/10.1016/j.smim.2007.11.004.

[3] H.G. Willert, H. Bertram, G.H. Buchhorn, Osteolysis in alloarthroplasty of the hip. The role of ultra-high molecular weight polyethylene wear particles, Clin. Orthop. Relat. Res. 258 (1990) 95–107, https://doi.org/10.1177/036354659001800518.

[4] J. Julin, E. Jamsen, T. Puolakka, Y.T. Konttinen, T. Moilanen, Younger age increases the risk of early prosthesis failure following primary total knee replacement for osteoarthritis. A follow-up study of 32,019 total knee replacements in the Finnish Arthroplasty Register, Acta Orthop. 81 (4) (2010) 413–419, https://doi.org/10.3109/17453674.2010.501747.

[5] S.M. Kurtz, E. Lau, K. Ong, K. Zhao, M. Kelly, K.J. Bozic, Future young patient demand for primary and revision joint replacement: national projections from 2010 to 2030, Clin. Orthop. Relat. Res. 467 (10) (2009) 2606–2612, https://doi.org/10.1007/s11999-009-0834-6.

[6] R.T. Beck, K.D. Illingworth, K.J. Saleh, Review of periprosthetic osteolysis in total joint arthroplasty: an emphasis on host factors and future directions, J. Orthop. Res. 30 (4) (2012) 541–546, https://doi.org/10.1002/jor.21554.

[7] I.R. Garrett, B.F. Boyce, R.O. Oreffo, L. Bonewald, J. Poser, G.R. Mundy, Oxygen-derived free radicals stimulate osteoclastic bone resorption in rodent bone in vitro and in vivo, J. Clin. Invest. 85 (3) (1990) 632–639, https://doi.org/10.1172/JCI114485.

[8] N.K. Lee, Y.G. Choi, J.Y. Baik, S.Y. Han, D.W. Jeong, Y.S. Bae, et al., A crucial role for reactive oxygen species in RANKL-induced osteoclast differentiation, Blood 106 (3) (2005) 852–859, https://doi.org/10.1182/blood-2004-09-3662.

[9] M.J. Steinbeck, L.J. Jablonowski, J. Parvizi, T.A. Freeman, The role of oxidative stress in aseptic loosening of total hip arthroplasties, J. Arthroplasty 29 (4) (2014) 843–849, https://doi.org/10.1016/j.arth.2013.09.001.

[10] S.B. Goodman, E. Gibon, J. Pajarinen, T.H. Lin, M. Keeney, P.G. Ren, et al., Novel biological strategies for treatment of wear particle-induced periprosthetic osteolysis of orthopaedic implants for joint replacement, J. R. Soc. Interface 11 (93) (2014) 20130962, https://doi.org/10.1098/rsif.2013.0962.

[11] P.E. Purdue, P. Koulouvaris, H.G. Potter, B.J. Nestor, T.P. Sculco, The cellular and molecular biology of periprosthetic osteolysis, Clin. Orthop. Relat. Res. 454 (2007) 251–261, https://doi.org/10.1097/01.blo.0000238813.95035.1b.

[12] J. Ouyang, X. Ji, X. Zhang, C. Feng, Z. Tang, N. Kong, et al., In situ sprayed NIR-responsive, analgesic black phosphorus-based gel for diabetic ulcer treatment, Proc. Natl. Acad. Sci. Unit. States Am. 117 (46) (2020) 28667–28677, https://doi.org/10.1073/pnas.2016268117.

[13] J. Yang, X. Zhang, C. Liu, Z. Wang, L. Deng, C. Feng, et al., Biologically modified nanoparticles as theranostic bionanomaterials, Prog. Mater. Sci. 118 (2021) 100768, https://doi.org/10.1016/j.pmatsci.2020.100768.

[14] X. Wei, B. Liu, G. Liu, F. Yang, F. Cao, X. Dou, et al., Mesenchymal stem cell-loaded porous tantalum integrated with biomimetic 3D collagen-based scaffold to repair large osteochondral defects in goats, Stem Cell Res. Ther. 10 (1) (2019) 72, https://doi.org/10.1186/s13287-019-1176-2.

[15] M. Hu, X. Lin, R. Huang, K. Yang, Y. Liang, X. Zhang, et al., Lightweight, highly permeable, biocompatible, and antiadhesive composite meshes for intraperitoneal repairs, Macromol. Biosci. 18 (7) (2018), e1800067, https://doi.org/10.1002/mabi.201800067.

[16] Z. Li, D. Chu, Y. Gao, L. Jin, X. Zhang, W. Cui, et al., Biomimicry, biomineralization, and bioregeneration of bone using advanced three-dimensional fibrous hydroxyapatite scaffold, Materials Today Advances 3 (2019) 100014, https://doi.org/10.1016/j.mtadv.2019.100014.

[17] J. Li, Z. Li, D. Chu, L. Jin, X. Zhang, Fabrication and biocompatibility of core–shell structured magnetic fibrous scaffold, J. Biomed. Nanotechnol. 15 (3) (2019) 500–506, https://doi.org/10.1166/jbn.2019.2701.

[18] S. Luo, S. Wu, J. Xu, X. Zhang, L. Zou, R. Yao, et al., Osteogenic differentiation of BMSCs on MoS2 composite nanofibers with different cell seeding densities, Appl. Nanosci. 10 (9) (2020) 3703–3716, https://doi.org/10.1007/s13204-020-01473-0.

[19] Z. Yang, D. Gao, X. Guo, L. Jin, J. Zheng, Y. Wang, et al., Fighting immune cold and reprogramming immunosuppressive tumor microenvironment with red blood cell membrane-camouflaged nanobullets, ACS Nano 14 (12) (2020) 17442–17457, https://doi.org/10.1021/acsnano.0c07721.

[20] Z. Tang, X. Zhang, Y. Shu, M. Guo, H. Zhang, W. Tao, Insights from nanotechnology in COVID-19 treatment, Nano Today 36 (2021) 101019, https://doi.org/10.1016/j.nantod.2020.101019.

[21] Z. Tang, N. Kong, X. Zhang, Y. Liu, P. Hu, S. Mou, et al., A materials-science perspective on tackling COVID-19, Nat Rev Mater (2020) 1–14, https://doi.org/10.1038/s41578-020-00247-y.

[22] K. Brieger, S. Schiavone, F.J. Miller Jr., K.H. Krause, Reactive oxygen species: from health to disease, Swiss Med. Wkly. 142 (2012) w13659, https://doi.org/10.4414/smw.2012.13659.

[23] X. Li, W. You, L. Wang, J. Liu, Z. Wu, K. Pei, et al., Self-assembly-magnetized MXene avoid dual-agglomeration with enhanced interfaces for strong microwave absorption through a tunable electromagnetic property, ACS Appl. Mater. Interfaces 11 (47) (2019) 44536–44544, https://doi.org/10.1021/acsami.9b11861.

[24] D. Wang, F. Li, R. Lian, J. Xu, D. Kan, Y. Liu, et al., A general atomic surface modification strategy for improving anchoring and electrocatalysis behavior of Ti3C2T2 MXene in lithium-sulfur batteries, ACS Nano 13 (10) (2019) 11078–11086, https://doi.org/10.1021/acsnano.9b03412.

[25] X. Fan, Y. Yang, X. Shi, Y. Liu, H. Li, J. Liang, et al., A MXene-based hierarchical design enabling highly efficient and stable solar-water desalination with good salt resistance, Adv. Funct. Mater. 30 (52) (2020) 2007110, https://doi.org/10.1002/adfm.202007110.

[26] R. Huang, X. Chen, Y. Dong, X. Zhang, Y. Wei, Z. Yang, et al., MXene composite nanofibers for cell culture and tissue engineering, ACS Applied Bio Materials 3 (4) (2020) 2125–2131, https://doi.org/10.1021/acsabm.0c00007.

[27] L. Jin, X. Guo, D. Gao, C. Wu, B. Hu, G. Tan, et al., NIR-responsive MXene nanobelts for wound healing, NPG Asia Mater. 13 (1) (2021) 24, https://doi.org/10.1038/s41427-021-00289-w.

[28] B. Xu, M. Zhu, W. Zhang, X. Zhen, Z. Pei, Q. Xue, et al., Ultrathin MXene-micropattern-based field-effect transistor for probing neural activity, Adv. Mater. 28 (17) (2016) 3333–3339, https://doi.org/10.1002/adma.201504657.

[29] H. Lin, X. Wang, L. Yu, Y. Chen, J. Shi, Two-Dimensional ultrathin MXene ceramic nanosheets for photothermal conversion, Nano Lett. 17 (1) (2017) 384–391, https://doi.org/10.1021/acs.nanolett.6b04339.

[30] X. Ren, M. Huo, M. Wang, H. Lin, X. Zhang, J. Yin, et al., Highly catalytic niobium carbide (MXene) promotes hematopoietic recovery after radiation by free radical scavenging, ACS Nano 13 (6) (2019) 6438–6454, https://doi.org/10.1021/acsnano.8b09327.

[31] K. Rasool, M. Helal, A. Ali, C.E. Ren, Y. Gogotsi, K.A. Mahmoud, Antibacterial activity of Ti(3)C(2)Tx MXene, ACS Nano 10 (3) (2016) 3674–3684, https://doi.org/10.1021/acsnano.6b00181.

[32] A. Jastrzebska, A. Szuplewska, A. Rozmysłowska-Wojciechowska, J. Mitrzak, T. Wojciechowski, M. Chudy, et al., Juggling surface charges of 2D niobium carbide MXenes for a reactive oxygen species scavenging and effective targeting of the malignant melanoma cell cycle into programmed cell death, ACS Sustain. Chem. Eng. 8 (21) (2020) 7942–7951, https://doi.org/10.1021/acssuschemeng.0c01609.

[33] G. Kresse, J. Furthmuller, Efficient iterative schemes for ab initio total-energy calculations using a plane-wave basis set, Phys. Rev. B Condens. Matter 54 (16) (1996) 11169–11186, https://doi.org/10.1103/physrevb.54.11169.

[34] C. Nich, A.J. Rao, R.D. Valladares, C. Li, J.E. Christman, J.K. Antonios, et al., Role of direct estrogen receptor signaling in wear particle-induced osteolysis, Biomaterials 34 (3) (2013) 641–650, https://doi.org/10.1016/j.biomaterials.2012.10.030.

[35] C. Wedemeyer, J. Xu, C. Neuerburg, S. Landgraeber, N.M. Malyar, F. von Knoch, et al., Particle-induced osteolysis in three-dimensional micro-computed tomography, Calcif. Tissue Int. 81 (5) (2007) 394–402, https://doi.org/10.1007/s00223-007-9077-2.

[36] S. Neampet, N. Ruecha, J. Qin, W. Wonsawat, O. Chailapakul, N. Rodthongkum, A nanocomposite prepared from platinum particles, polyaniline and a Ti3C2 MXene for amperometric sensing of hydrogen peroxide and lactate, Mikrochim. Acta 186 (12) (2019) 752, https://doi.org/10.1007/s00604-019-3845-3.

[37] A. Djire, A. Bos, J. Liu, H. Zhang, E.M. Miller, N.R. Neale, Pseudocapacitive storage in nanolayered Ti2NTx MXene using Mg-ion electrolyte, ACS Applied Nano Materials 2 (5) (2019) 2785–2795, https://doi.org/10.1021/acsanm.9b00289.

[38] L.J. Liu, Q. Zhao, R. Liu, L.F. Zhu, Hydrogen adsorption-induced catalytic enhancement over Cu nanoparticles immobilized by layered Ti3C2 MXene, Appl. Catal. B Environ. 252 (2019) 198–204, https://doi.org/10.1016/j.apcatb.2019.04.026.

[39] S. Tu, F. Ming, J. Zhang, X. Zhang, H.N. Alshareef, MXene-derived ferroelectric crystals, Adv. Mater. 31 (14) (2019), e1806860, https://doi.org/10.1002/adma.201806860.

[40] E.H. Martins Ferreira, M.V.O. Moutinho, F. Stavale, M.M. Lucchese, R.B. Capaz, C. A. Achete, et al., Evolution of the Raman spectra from single-, few-, and many-layer graphene with increasing disorder, Phys. Rev. B 82 (12) (2010) 125429, https://doi.org/10.1103/PhysRevB.82.125429.

[41] S. Huang, V.N. Mochalin, Understanding chemistry of two-dimensional transition metal carbides and carbonitrides (MXenes) with gas analysis, ACS Nano 14 (8) (2020) 10251–10257, https://doi.org/10.1021/acsnano.0c03602.
[42] M. Benchakar, L. Loupias, C. Garnero, T. Bilyk, C. Morais, C. Canaff, et al., One MAX phase, different MXenes: a guideline to understand the crucial role of etching conditions on Ti3C2Tx surface chemistry, Appl. Surf. Sci. 530 (2020) 147209, https://doi.org/10.1016/j.apsusc.2020.147209.
[43] H. Xiang, H. Lin, L. Yu, Y. Chen, Hypoxia-irrelevant photonic thermodynamic cancer nanomedicine, ACS Nano 13 (2) (2019) 2223–2235, https://doi.org/10.1021/acsnano.8b08910.
[44] W. Tang, E. Sanville, G. Henkelman, A grid-based Bader analysis algorithm without lattice bias, J. Phys. Condens. Matter 21 (8) (2009), 084204, https://doi.org/10.1088/0953-8984/21/8/084204.
[45] Y. Wu, X. Zhou, M. Li, Y. Wang, B. Zhou, N. Wu, et al., 2D/3D interface engineering: direct Z-scheme g-C3N4/YMnO3 heterojunction for reinforced visible-light photocatalytic oxidation, J. Mater. Sci. Mater. Electron. 30 (19) (2019) 17601–17611, https://doi.org/10.1007/s10854-019-02109-y.
[46] X. Han, X. Jing, D. Yang, H. Lin, Z. Wang, H. Ran, et al., Therapeutic mesopore construction on 2D Nb2C MXenes for targeted and enhanced chemo-photothermal cancer therapy in NIR-II biowindow, Theranostics 8 (16) (2018) 4491–4508, https://doi.org/10.7150/thno.26291.
[47] M. Dos-Santos-Pereira, F.S. Guimaraes, E. Del-Bel, R. Raisman-Vozari, P.P. Michel, Cannabidiol prevents LPS-induced microglial inflammation by inhibiting ROS/NF-kappaB-dependent signaling and glucose consumption, Glia 68 (3) (2020) 561–573, https://doi.org/10.1002/glia.23738.
[48] P. Zhang, Y. Yin, T. Wang, W. Li, C. Li, X. Zeng, et al., Maresin 1 mitigates concanavalin A-induced acute liver injury in mice by inhibiting ROS-mediated activation of NF-kappaB signaling, Free Radic. Biol. Med. 147 (2020) 23–36, https://doi.org/10.1016/j.freeradbiomed.2019.11.033.
[49] R. Guo, M. Xiao, W. Zhao, S. Zhou, Y. Hu, M. Liao, et al., 2D Ti3C2TxMXene couples electrical stimulation to promote proliferation and neural differentiation of neural stem cells, Acta Biomater. (2020), https://doi.org/10.1016/j.actbio.2020.12.035. In press.
[50] L. Zhou, H. Zheng, Z. Liu, S. Wang, Z. Liu, F. Chen, et al., Conductive antibacterial hemostatic multifunctional scaffolds based on Ti3C2Tx MXene nanosheets for promoting multidrug-resistant bacteria-infected wound healing, ACS Nano 15 (2) (2021) 2468–2480, https://doi.org/10.1021/acsnano.0c06287.
[51] J. Takito, S. Inoue, M. Nakamura, The sealing zone in osteoclasts: a self-organized structure on the bone, Int. J. Mol. Sci. 19 (4) (2018) 984, https://doi.org/10.3390/ijms19040984.
[52] B.G. Darnay, V. Haridas, J. Ni, P.A. Moore, B.B. Aggarwal, Characterization of the intracellular domain of receptor activator of NF-kappaB (RANK). Interaction with tumor necrosis factor receptor-associated factors and activation of NF-kappab and c-Jun N-terminal kinase, J. Biol. Chem. 273 (32) (1998) 20551–20555, https://doi.org/10.1074/jbc.273.32.20551.
[53] E.M. Greenfield, Y. Bi, A.A. Ragab, V.M. Goldberg, R.R. Van De Motter, The role of osteoclast differentiation in aseptic loosening, J. Orthop. Res. 20 (1) (2002) 1–8, https://doi.org/10.1016/S0736-0266(01)00070-5.
[54] A. Nakanishi, M. Hie, N. Iitsuka, I. Tsukamoto, A crucial role for reactive oxygen species in macrophage colony-stimulating factor-induced RANK expression in osteoclastic differentiation, Int. J. Mol. Med. 31 (4) (2013) 874–880, https://doi.org/10.3892/ijmm.2013.1258.
[55] H. Lin, S. Gao, C. Dai, Y. Chen, J. Shi, A two-dimensional biodegradable niobium carbide (MXene) for photothermal tumor eradication in NIR-I and NIR-II biowindows, J. Am. Chem. Soc. 139 (45) (2017) 16235–16247, https://doi.org/10.1021/jacs.7b07818.
[56] C. Bratengeier, A.D. Bakker, A. Fahlgren, Mechanical loading releases osteoclastogenesis-modulating factors through stimulation of the P2X7 receptor in hematopoietic progenitor cells, J. Cell. Physiol. 234 (8) (2019) 13057–13067, https://doi.org/10.1002/jcp.27976.
[57] Y. Tamaki, Y. Takakubo, K. Goto, T. Hirayama, K. Sasaki, Y.T. Konttinen, et al., Increased expression of toll-like receptors in aseptic loose periprosthetic tissues and septic synovial membranes around total hip implants, J. Rheumatol. 36 (3) (2009) 598–608, https://doi.org/10.3899/jrheum.080390.
[58] R. Maitra, C.C. Clement, G.M. Crisi, N. Cobelli, L. Santambrogio, Immunogenecity of modified alkane polymers is mediated through TLR1/2 activation, PloS One 3 (6) (2008) e2438, https://doi.org/10.1371/journal.pone.0002438.
[59] A. Vargas-Caraveo, A. Sayd, S.R. Maus, J.R. Caso, J.L.M. Madrigal, B. Garcia-Bueno, et al., Lipopolysaccharide enters the rat brain by a lipoprotein-mediated transport mechanism in physiological conditions, Sci. Rep. 7 (1) (2017) 13113, https://doi.org/10.1038/s41598-017-13302-6.